Proceedings of the EuroGNC 2013, 2nd CEAS Specialist Conference
on Guidance, Navigation & Control, Delft University of Technology,
Delft, The Netherlands, April 10-12, 2013

Aeroservoelastic Investigations of a High-Aspect-Ratio Motor Glider

Flávio Silvestre

Abstract This paper presents aeroservoelastic investigations for the STEMME S15 prototype using a methodology of modelling the flexible aircraft dynamics in the time domain. The effects of the flexibility in the closed-loop stability according to the sensor positioning are discussed, for a pitch and a yaw damper. The modelling of the flexible dynamics is based on the mean axes approximation, without considering the inertial coupling between the rigid-body and the elastic degrees of freedom. The structural dynamics is linearly represented in modal coordinates. To determine the incremental aerodynamics due to elastic deformations, an unsteady strip theory formulation in the time domain is used, considering the exponential representation of the Wagner function and the resulting stripwise aerodynamic lag states. Spanwise correction to account for three-dimensional effects at the wing tip based on the quasi-steady circulation distribution was applied. The validation of the open-loop flexible aircraft simulations with flight test results are also presented.

1 Introduction

The use of aircraft control associated with aeroelasticity, or the inclusion of aeroelastic effects on the aircraft control design, gave rise to a new terminology, frequently used in the last years in aeronautical engineering: Aero**servo**elasticity. In the editorial of a special issue of the AIAA Journal of Aircraft about the Active Flexible Wing Program [5], Noll and Eastep [4] outlined the increasing importance of aeroelasticity and aeroservoelasticity in the vehicle conceptual and preliminary design process. Nowadays aeroservoelastic stability analyses are required for clearance of flight control laws either if the control laws are designed for influencing aeroelastic behaviour, such as flutter suppression functions, or if they are designed for manual or automatic flight control of the aircraft. Complex models of the flexible aircraft

Flávio Silvestre
Instituto Tecnológico de Aeronáutica, São José dos Campos, Brazil e-mail: flaviojs@ita.br

dynamics that integrate CFD (computational fluid dynamics) and FEM (finite element method) codes have been developed for open-loop and closed-loop simulation and analysis, but they require very much computing time. Moreover, the complexity of CFD/FEM models still hampers their usage in flight control system design [13].

Even in major aircraft industries, integrated aeroelastic models are still only applied for flight control validation, and not in the flight control system development. A schematic flow chart representing the industrial flight control law design process is shown in ref. [10], based on Fielding and Luckner [7] considerations, indicating that aeroservoelastic analyses are carried out only after the off-line design. The costs associated with these methods are also very high, inhibiting their application by small aircraft industries. According to Krüger [9], it is (also) necessary to offer faster and cheaper processes for the stability analysis of small, sport class of aircraft.

In this scenario, simpler but still reliable models for aeroservoelastic applications are desired. To fulfil these demands, a novel methodology for modelling the dynamics of slightly flexible, high-aspect-ratio aircraft in the time domain has been developed by Silvestre [16]. The objective of this paper is to demonstrate how the effects of the flexibility can be taken into account in flight control law design using this methodology. For this, the examples of a yaw damper and a pitch damper for the STEMME S15 are considered, and the effects of the flexibility according to the angular rates sensor position are demonstrated. In section 2 the methodology is presented; section 3 details the S15; subsequently the validation of the methodology is commented on in section 4; the aeroservoelastic investigations are discussed in section 5, and finally the most important points are summarised in section 6 completing the scope of this paper.

2 The Flexible Dynamics Model

Within the project LAPAZ a non-linear high-fidelity flight simulation model for the rigid aircraft, the motor glider STEMME S15, was built up in MATLAB® Simulink environment at TUB, as described by Meyer-Brügel in [15]. This complete and complex model involves the six-degrees-of-freedom equations of motion with quaternion based attitude calculation, considering the earth's rotation and defining the earth as an ellipsoid. Not only the body flight dynamics was modelled, but also the dynamics of various systems composing the aircraft, the power plant dynamics, the dynamics of all actuators for all control surfaces and for the engine, the landing gear and the nose wheel actuation, and the dynamics of all sensors installed on the aircraft that are used for generating inputs to the flight control system. The model is also equipped with a terrain model, necessary to validate the flight control laws at low level flight. The aircraft is considered as a rigid body.

The calculation of "rigid-body"[1] aerodynamic forces and moments is based on parameter identification, assuming the aerodynamic force and moment coefficients to be represented by parametric polynomial equations. The equations have a maximal polynomial rank of three and contain cross coupling terms up to second order. The parameters have been estimated from flight test results utilizing parameter identification methods. For the concerned aircraft class an extensive flight test campaign was conducted, involving 16 different manoeuvre types which have been realised in 16 different reference flight conditions. Overall, approximately 40 GB of data was generated, analysed and evaluated by Meyer-Brügel [15]. The most important variables of the identified non-linear aerodynamic model are the angle of attack, sideslip angle, angular rates, aerodynamic control surfaces deflections and motor rotation. The model takes also into account ground effect and stall.

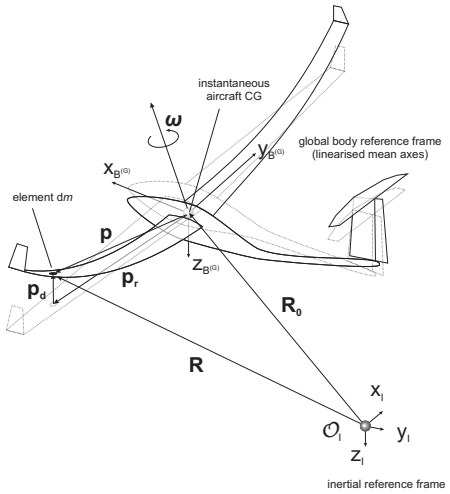

Fig. 1 Flying flexible aircraft, and the inertial and mean axes reference frames.

To account for the aeroelasticity, a methodology was developed by Silvestre [16] to extend the rigid-body simulation model. This methodology is based on the equations of motion for slightly flexible aircraft, derived at the reference system of the so called mean axes, as explained in ref. [3]. The mean axes are defined as a floating reference frame where the linear and angular momenta caused by elastic deformations vanish [2]. For slightly flexible aircraft, small structural displacements can be assumed, and linearised mean axes constraints can be applied instead. Using the modal approach to model the structural dynamics, the linearised mean axes are found to lay at the centre of gravity (CG) of the undeformed structure, as in Fig. 1.

Applying Lagrangian mechanics, the use of the modal approach and the practical mean axes constraints lead to the final equations of motion of the flexible aircraft. These equations are formally the rigid-body equations of motion, supplemented by

[1] "Rigid-body" aerodynamics refers to the aerodynamic forces and moments resulting from global change of the aircraft state, regardless the changes caused by the flexible displacements.

the differential equations of the structural dynamics in modal coordinates (the modal amplitudes). The hypothesis of small elastic displacements results in no inertial coupling among the flight dynamics and the structural dynamics. The only coupling is of an aerodynamic nature.

The unsteady incremental aerodynamic forces and moments are modelled using the incompressible potential theory. Jones' exponential approximation of the Wagner function [1] is used to model the circulatory contribution in the time domain. The strip theory is applied, and the quasi-steady circulation distribution is used to account for three-dimensional effects. Working with n_e elastic modes in the model, which may be determined in a ground vibration test or calculated using a finite-element model of the aircraft structure, each elastic mode is linearised at the elastic axis (EA) of the lifting surface, as shown in Fig. 2.

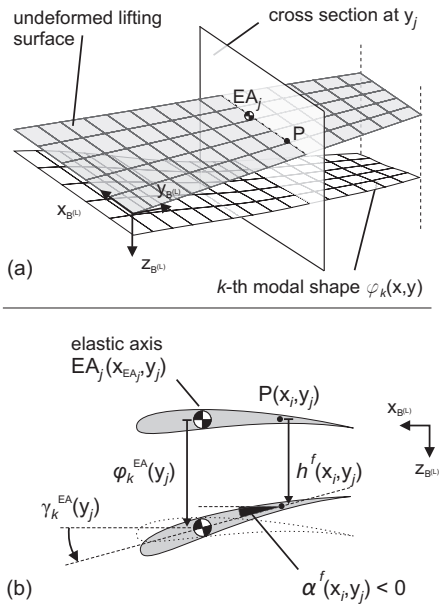

Fig. 2 Approximation of the elastic modal shapes at the elastic axis by equivalent displacement and torsion: (a) representation of the k-th modal shape on the LBRF; (b) cross section y_j.

Considering both the non-circulatory (NC) and the circulatory (C) contributions, the incremental aerodynamic forces $\mathbf{F}_{\mathrm{A}}|_{\mathrm{B}^{(\mathrm{G})}}$ and moments $\mathbf{M}_{\mathrm{A}}|_{\mathrm{B}^{(\mathrm{G})}}$ can be written as:

$$\begin{aligned}\mathbf{F}_{\mathrm{A}}|_{\mathrm{B}^{(\mathrm{G})}}(t) = {} & \rho(t)\mathbf{F}_{\mathrm{A}\ddot{\boldsymbol{\eta}}}(t)\ddot{\boldsymbol{\eta}}(t) \\ & +\rho(t)V(t)\mathbf{F}_{\mathrm{A}\dot{\boldsymbol{\eta}}}(t)\dot{\boldsymbol{\eta}}(t) \\ & +\rho(t)V^2(t)\mathbf{F}_{\mathrm{A}\boldsymbol{\eta}}(t)\boldsymbol{\eta}(t) \\ & +\rho(t)V(t)\mathbf{F}_{\mathrm{A}\boldsymbol{\lambda}}(t)\left(\boldsymbol{\lambda}_1(t)+\boldsymbol{\lambda}_2(t)\right), \end{aligned} \tag{1}$$

$$\begin{aligned}\mathbf{M}_{\mathrm{A}}|_{\mathrm{B}^{(\mathrm{G})}}(t) = &\rho(t)\mathbf{M}_{\mathrm{A}\ddot{\boldsymbol{\eta}}}(t)\ddot{\boldsymbol{\eta}}(t)\\ &+\rho(t)V(t)\mathbf{M}_{\mathrm{A}\dot{\boldsymbol{\eta}}}(t)\dot{\boldsymbol{\eta}}(t)\\ &+\rho(t)V^2(t)\mathbf{M}_{\mathrm{A}\boldsymbol{\eta}}(t)\boldsymbol{\eta}(t)\\ &+\rho(t)V(t)\mathbf{M}_{\mathrm{A}\boldsymbol{\lambda}}(t)\left(\boldsymbol{\lambda}_1(t)+\boldsymbol{\lambda}_2(t)\right).\end{aligned} \tag{2}$$

The generalised force at the *k*-th elastic mode can be similarly put into the form:

$$\begin{aligned}Q_{\eta_k}(t) = &\rho(t)\mathbf{Q}_{\eta_k\ddot{\boldsymbol{\eta}}}(t)\ddot{\boldsymbol{\eta}}(t)\\ &+\rho(t)V(t)\mathbf{Q}_{\eta_k\dot{\boldsymbol{\eta}}}(t)\dot{\boldsymbol{\eta}}(t)\\ &+\rho(t)V^2(t)\mathbf{Q}_{\eta_k\boldsymbol{\eta}}(t)\boldsymbol{\eta}(t)\\ &+\rho(t)V(t)\mathbf{Q}_{\eta_k\boldsymbol{\lambda}}(t)\left(\boldsymbol{\lambda}_1(t)+\boldsymbol{\lambda}_2(t)\right).\end{aligned} \tag{3}$$

wherein ρ is the air density, V is the true airspeed, $\boldsymbol{\eta}$ is the vector of the modal amplitudes, $\boldsymbol{\lambda_1}$ and $\boldsymbol{\lambda_2}$ are the vectors of the stripwise first and second lag states, according to the exponential approximation of the Wagner function. The twelve matrix coefficients in Equations (1), (2) and (3) are determined in ref. [16]

The equations of motion of the flexible aircraft are summarised in the following. The matrices used in Equations from (5) to (7) are defined according to Tab. 1.

- Equations of the flight dynamics:

$$\begin{aligned}\dot{\mathbf{V}}\big|_{\mathrm{B}^{(\mathrm{G})}}(t) &= -\boldsymbol{\omega}|_{\mathrm{B}^{(\mathrm{G})}}(t)\times\mathbf{V}|_{\mathrm{B}^{(\mathrm{G})}}(t)+\mathbf{T}_{\mathrm{B}^{(\mathrm{G})}\mathrm{I}}(t)\,\mathbf{G}|_{\mathrm{I}}+\tfrac{1}{m}\,\mathbf{F}^{\mathrm{ext}}\big|_{\mathrm{B}^{(\mathrm{G})}}(t)\\ \dot{\boldsymbol{\omega}}|_{\mathrm{B}^{(\mathrm{G})}}(t) &= -\mathbf{J}^{-1}\left(\boldsymbol{\omega}|_{\mathrm{B}^{(\mathrm{G})}}(t)\times\left(\mathbf{J}\,\boldsymbol{\omega}|_{\mathrm{B}^{(\mathrm{G})}}(t)\right)\right)+\mathbf{J}^{-1}\,\mathbf{M}^{\mathrm{ext}}\big|_{\mathrm{B}^{(\mathrm{G})}}(t),\end{aligned} \tag{4}$$

wherein $\mathbf{F}^{\mathrm{ext}}|_{\mathrm{B}^{(\mathrm{G})}}$ and $\mathbf{M}^{\mathrm{ext}}|_{\mathrm{B}^{(\mathrm{G})}}$ are the external (propulsion and aerodynamic) forces and moments acting over the aircraft, including the forces and moments caused by the aircraft elasticity; $\mathbf{G}|_{\mathrm{I}}$ is the gravity acceleration vector($\begin{bmatrix}0 & 0 & g\end{bmatrix}^T$), m is the aircraft mass and $\mathbf{J}$ is the aircraft inertia matrix; $\mathbf{T}_{\mathrm{B}^{(\mathrm{G})}\mathrm{I}}$ is the transformation matrix from the inertial to the global body reference frame; $\mathbf{V}|_{\mathrm{B}^{(\mathrm{G})}}$ and $\boldsymbol{\omega}|_{\mathrm{B}^{(\mathrm{G})}}$ are respectively the aircraft linear and angular velocities relative to the inertial reference system but written on the global body reference frame.

- Equations of the structural dynamics:

$$\begin{bmatrix}\dot{\boldsymbol{\eta}}(t)\\ \ddot{\boldsymbol{\eta}}(t)\end{bmatrix} = \begin{bmatrix}\mathbf{0}_{n_e\times n_e} & \mathbf{I}_{n_e\times n_e}\\ \boldsymbol{\Pi}_1(t) & \boldsymbol{\Pi}_2(t)\end{bmatrix}\begin{bmatrix}\boldsymbol{\eta}(t)\\ \dot{\boldsymbol{\eta}}(t)\end{bmatrix} + \begin{bmatrix}\mathbf{0}_{n_e\times n_e}\\ \boldsymbol{\Pi}_3(t)\end{bmatrix}(\boldsymbol{\lambda}_1(t)+\boldsymbol{\lambda}_2(t)) + \begin{bmatrix}\mathbf{0}_{n_e\times n_e}\\ \boldsymbol{\Pi}_4(t)\end{bmatrix}\mathbf{X}_{\text{state}}(t) + \begin{bmatrix}\mathbf{0}_{n_e\times n_e}\\ \boldsymbol{\Pi}_5(t)\end{bmatrix}\mathbf{u}_{\text{control}}(t). \quad (5)$$

The matrices $\boldsymbol{\Pi}_1$, $\boldsymbol{\Pi}_2$, $\boldsymbol{\Pi}_3$, $\boldsymbol{\Pi}_4$ and $\boldsymbol{\Pi}_5$ are defined as:

$$\begin{aligned}
\boldsymbol{\Pi}_1(t) &= \left[\boldsymbol{\mu} - \rho(t)\mathbf{Q}_{\boldsymbol{\eta}\ddot{\boldsymbol{\eta}}}^{(\text{NC})}(t)\right]^{-1}\left[-\boldsymbol{\mu}\boldsymbol{\omega}_n^2 + \rho(t)V^2(t)\left(\mathbf{Q}_{\boldsymbol{\eta}\boldsymbol{\eta}}^{(\text{NC})}(t) + \mathbf{Q}_{\boldsymbol{\eta}\boldsymbol{\eta}}^{(\text{C})}(t)\right)\right]\\
\boldsymbol{\Pi}_2(t) &= \left[\boldsymbol{\mu} - \rho(t)\mathbf{Q}_{\boldsymbol{\eta}\ddot{\boldsymbol{\eta}}}^{(\text{NC})}(t)\right]^{-1}\left[-2\boldsymbol{\mu}\boldsymbol{\xi}\boldsymbol{\omega}_n + \rho(t)V(t)\left(\mathbf{Q}_{\boldsymbol{\eta}\dot{\boldsymbol{\eta}}}^{(\text{NC})}(t) + \mathbf{Q}_{\boldsymbol{\eta}\dot{\boldsymbol{\eta}}}^{(\text{C})}(t)\right)\right]\\
\boldsymbol{\Pi}_3(t) &= \left[\boldsymbol{\mu} - \rho(t)\mathbf{Q}_{\boldsymbol{\eta}\ddot{\boldsymbol{\eta}}}^{(\text{NC})}(t)\right]^{-1}\rho(t)V(t)\mathbf{Q}_{\boldsymbol{\eta}\boldsymbol{\lambda}}^{(\text{NC})}(t)\\
\boldsymbol{\Pi}_4(t) &= \left[\boldsymbol{\mu} - \rho(t)\mathbf{Q}_{\boldsymbol{\eta}\ddot{\boldsymbol{\eta}}}^{(\text{NC})}(t)\right]^{-1}\frac{1}{2}\rho(t)V^2(t)S\bar{c}\mathbf{Q}_{\boldsymbol{\eta}\mathbf{X}_{\text{state}}}^{(\text{QS})}(t)\\
\boldsymbol{\Pi}_5(t) &= \left[\boldsymbol{\mu} - \rho(t)\mathbf{Q}_{\boldsymbol{\eta}\ddot{\boldsymbol{\eta}}}^{(\text{NC})}(t)\right]^{-1}\frac{1}{2}\rho(t)V^2(t)S\bar{c}\mathbf{Q}_{\boldsymbol{\eta}\mathbf{u}_{\text{control}}}^{(\text{QS})}(t). \quad (6)
\end{aligned}$$

In the latter Equations (5) and (6), $\mathbf{I}_{n_e\times n_e}$ and $\mathbf{0}_{n_e\times n_e}$ are respectively the identity and the null matrices of order n_e; $\mathbf{Q}_{\boldsymbol{\eta}\mathbf{X}_{\text{state}}}^{(\text{QS})}$ and $\mathbf{Q}_{\boldsymbol{\eta}\mathbf{u}_{\text{control}}}^{(\text{QS})}$ are respectively the contribution of the aircraft state and the deflection of the control surfaces to the elastic generalised loads, which were assumed to be quasi-stationary in this work. They are calculated with quasi-steady aerodynamics and the strip theory, as in ref. [11]. The elements of the state vector $\mathbf{X}_{\text{state}}$ are the aircraft angle of attack α, sideslip angle β, and the non-dimensional (divided by the factor $V/\left(\frac{\bar{c}}{2}\right)$) angular rates $\bar{p}$, $\bar{q}$, and $\bar{r}$; the elements of the control vector $\mathbf{u}_{\text{control}}$ are the deflection of the control surfaces: aileron, elevator, flaps, and rudder. Refer to ref. [11] for the expressions of the structural stability derivatives in $\mathbf{Q}_{\boldsymbol{\eta}\mathbf{X}_{\text{state}}}^{(\text{QS})}$ and $\mathbf{Q}_{\boldsymbol{\eta}\mathbf{u}_{\text{control}}}^{(\text{QS})}$.

- Equations of the aerodynamic lag states:

$$\begin{aligned}
\dot{\boldsymbol{\lambda}}_1(t) &= 2V(t)a_1\boldsymbol{c}^{-1}\boldsymbol{\lambda}_1(t) + A_1\dot{\mathbf{w}}_{3/4}^f(t)\\
\dot{\boldsymbol{\lambda}}_2(t) &= 2V(t)a_2\boldsymbol{c}^{-1}\boldsymbol{\lambda}_2(t) + A_2\dot{\mathbf{w}}_{3/4}^f(t), \quad (7)
\end{aligned}$$

wherein $\dot{\mathbf{w}}_{3/4}^f(t)$ is the vector collecting the stripwise accelerations at the three-quarter-chord, which can be determined with the time derivative of the spanwise downwash at the three-quarter-chord, calculated in Eq. (8). It is a function of the modal amplitudes, velocities and accelerations, as well as the aircraft velocity:

$$\begin{aligned}
w_{3/4}^f(y_j,t) &= \boldsymbol{\varphi}^{\text{EA}}(y_j)\dot{\boldsymbol{\eta}}(t) - V(t)\boldsymbol{\gamma}^{\text{EA}}(y_j)\boldsymbol{\eta}(t) + \left(x_{3/4_j} - x_{\text{EA}_j}\right)\boldsymbol{\gamma}^{\text{EA}}(y_j)\dot{\boldsymbol{\eta}}(t)\\
&= \left[\boldsymbol{\varphi}^{\text{EA}}(y_j) + \left(x_{3/4_j} - x_{\text{EA}_j}\right)\boldsymbol{\gamma}^{\text{EA}}(y_j)\right]\dot{\boldsymbol{\eta}}(t) - V(t)\boldsymbol{\gamma}^{\text{EA}}(y_j)\boldsymbol{\eta}(t), \quad (8)
\end{aligned}$$

wherein $\boldsymbol{\varphi}^{\mathrm{EA}}$ and $\boldsymbol{\gamma}^{\mathrm{EA}}$ are respectively the vectors equivalent displacement and torsion at the lifting surface's elastic axis of all considered elastic modes.

Table 1 Matrix definitions in the aeroelastic model.

Matrix	Definition	Dimension
$\boldsymbol{\mu}$	diagonal matrix, containing the modal mass μ_k in the main diagonal (modal mass matrix)	$n_e \times n_e$
$\boldsymbol{\xi}$	diagonal matrix, containing the structural damping factors ξ_k in the main diagonal	$n_e \times n_e$
$\boldsymbol{\omega}_n$	diagonal matrix, containing the natural frequencies ω_{nk} in the main diagonal	$n_e \times n_e$
$\mathbf{0}_{n_e \times n_e}$	null matrix	$n_e \times n_e$
$\mathbf{I}_{n_e \times n_e}$	identity matrix	$n_e \times n_e$
$\mathbf{Q}_{\boldsymbol{\eta}\,\boldsymbol{\eta}}^{(\mathrm{NC})}, \mathbf{Q}_{\boldsymbol{\eta}\,\dot{\boldsymbol{\eta}}}^{(\mathrm{NC})}, \mathbf{Q}_{\boldsymbol{\eta}\,\ddot{\boldsymbol{\eta}}}^{(\mathrm{NC})}$	diagonal matrices, containing respectively the line vectors $\mathbf{Q}_{\eta_k\,\boldsymbol{\eta}}^{(\mathrm{NC})}, \mathbf{Q}_{\eta_k\,\dot{\boldsymbol{\eta}}}^{(\mathrm{NC})}, \mathbf{Q}_{\eta_k\,\ddot{\boldsymbol{\eta}}}^{(\mathrm{NC})}$	$n_e \times n_e$
$\mathbf{Q}_{\boldsymbol{\eta}\,\dot{\boldsymbol{\eta}}}^{(\mathrm{C})}, \mathbf{Q}_{\boldsymbol{\eta}\,\ddot{\boldsymbol{\eta}}}^{(\mathrm{C})}$	diagonal matrices, containing respectively the line vectors $\mathbf{Q}_{\eta_k\,\dot{\boldsymbol{\eta}}}^{(\mathrm{C})}, \mathbf{Q}_{\eta_k\,\ddot{\boldsymbol{\eta}}}^{(\mathrm{C})}$	$n_e \times n_e$
$\mathbf{Q}_{\boldsymbol{\eta}\,\boldsymbol{\lambda}}^{(\mathrm{C})}$	diagonal matrix, containing the line vectors $\mathbf{Q}_{\eta_k\,\boldsymbol{\lambda}}^{(\mathrm{C})}$	$n_e \times n_s$
$\mathbf{Q}_{\boldsymbol{\eta}\,\mathbf{X}_{\mathrm{state}}}^{(\mathrm{QS})}$	quasi-stationary contribution of aircraft states to the elastic generalised loads, considering $\mathbf{X}_{\mathrm{state}} = \begin{bmatrix} 1 & \alpha & \beta & \bar{p} & \bar{q} & \bar{r} \end{bmatrix}^T$ (see ref. [11])	$n_e \times 6$
$\mathbf{Q}_{\boldsymbol{\eta}\,\mathbf{u}_{\mathrm{control}}}^{(\mathrm{QS})}$	quasi-stationary contribution of the control surfaces to the elastic generalised loads, considering aileron, flaps, elevator and rudder (see ref. [11])	$n_e \times 4$
$\boldsymbol{\Pi}_1, \boldsymbol{\Pi}_2, \boldsymbol{\Pi}_3, \boldsymbol{\Pi}_4, \boldsymbol{\Pi}_5$	see Eq.(6)	$n_e \times n_e$
$\mathbf{c}$	diagonal matrix, containing the chords of all strips, c_j, in the main diagonal	$n_s \times n_s$
$\dot{\mathbf{w}}_{3/4}^{f}$	column vector which collects the downwash accelerations at the three-quarter-chord position of all strips	$n_s \times 1$

Together with the equations of the kinematics of flight, Equations (4), (5) and (7) are already in the form to be programmed for flight simulations of the flexible aircraft. Next section shows the integration of the aeroelastic model to the rigid-body flight simulation model of S15 prototype.

3 Aircraft Description

The modelling methodology of ref. [16], summarised in the last section, is applied to the STEMME S15 "Demonstrator", a prototype of the commercial motor glid-

ers STEMME S6 and S15[2] from the German aircraft manufacturer STEMME AG[3]. Having a higher wing stiffness than the production aircraft, the S15 prototype is an experimental aircraft platform that is used in the project LAPAZ (abbreviation for ***L**uft-**A**rbeits-**P**lattform für die **A**llgemeine **Z**ivilluftfahrt* in German, translated as aerial work platform for the general civil aviation), a project financially supported by the German National Aeronautics Research Programme (LuFo IV, abbreviation for ***Lu**ftfahrt**fo**rschungsprogramm* IV). In its first phase, the project intended to develop and demonstrate a reliable, high-precision automatic flight control system for the S15 to support measurements in flight for geo-exploration and surveillance tasks. The partners are the German aircraft manufacturer STEMME, the Universität Stuttgart and the Technische Universität Berlin (TUB), TUB being responsible for the flight simulation models as well as the flight control law design for the automatic flight control system. The first project phase, LAPAZ I[4], ended in October 2010 with flight tests, which proved that the flight control system had been successfully implemented. In a second phase, LAPAZ II[5], inaugurated in October 2010, automatic take-off and landing as well as gust load alleviation functions will be demonstrated. The landing function having already been successfully demonstrated by the end of March 2012, see ref. [17].

Fig. 3 The STEMME S15 prototype used in the LAPAZ project at Strausberg Airport.

The S15 is a utility aircraft, for which an optionally piloted version is being developed. It is equipped with a Bombardier-Rotax motor 914S, tricycle landing gear, and has two seats. The wing span is 18m and the horizontal empennage is in T-tail configuration. Figure 3 shows the aircraft at the aerodrome of Strausberg, Germany. The main properties are listed in ref. [17], and a summary is presented in Tab. 2 for

[2] S6 is the CS-22 certified sport version of the aircraft; S15 is the CS-23 certified utility aircraft with increased MTOW and hard points under the wings that allow mounting pods.

[3] Further information about the aircraft manufacturer at:
http://www.stemme.de

[4] Further information at TU Berlin's website of the project (February 2nd, 2012):
http://www.fmra.tu-berlin.de/menue/forschung/projekte/flugregelung/lapaz_i/

[5] Further information at TU Berlin's website of the project (March 8th, 2012):
http://www.fmra.tu-berlin.de/menue/forschung/projekte/flugregelung/lapaz_ii/

the aircraft empty configuration. The inertia moments were determined experimentally using a pendulum and techniques of system identification by Rudenko [14]. The inertia products I_{xy}, I_{xz} and I_{yz} were not estimated and thus considered null in a first approximation. The position of the centre of gravity in Tab. 2 was estimated as well in ref. [14], with the exception of the lateral position, approximated by zero assuming symmetry relative to the *xz*-plane.

Table 2 General properties of S15 "Demonstrator" in empty configuration (without pilot, co-pilot, and fuel).

Property	Symbol	Value	Unit
reference area	S	17.40	m^2
wing's mean aerodynamic chord	$\bar{c}$	1.0064	m
wing's span	b	18.0	m
mass (empty)	m	750	kg
inertia moment, x	I_{xx}	5262	$kg.m^2$
inertia moment, y	I_{yy}	1913	$kg.m^2$
inertia moment, z	I_{zz}	7015	$kg.m^2$
position of the CG, x	x_{CG}	-2.8070	m
position of the CG, y	x_{CG}	0	m
position of the CG, z	x_{CG}	-0.2640	m

The S15 demonstrator has a stall speed at MTOW of approximately 90.0km/h (25.0m/s), and a maximum speed in level flight with maximum continuous power of approximately 280.0km/h (77.8m/s).

As discussed in section 2, the structural dynamics in the aeroelastic model are represented using the modal approach. The Institute of Reliability (*Institut für Zuverlässigkeitstechnik*) of the Technical University Hamburg-Harburg (TUHH) carried out a GVT (Ground Vibration Test) campaign with the S15 in 2008 for flutter calculations [12]. This work uses the available results. For the aeroelastic model, the modal eigenvectors up to 30Hz were considered, which are given in Tab. 3. This is assumed to be sufficient for the intended investigations that address aeroservoelastic effects of the controlled aircraft. Table 3 refers to the fixed-control-surface GVT results[6].

Figure 4 shows the linearised modal shape of the first symmetric wing torsion together with the points obtained at the GVT, where the accelerations were measured. Observe that just the modal shape's component perpendicular to the lifting surface, thus the only component considered in the incremental aerodynamic model, is displayed. The linearised modal shape fits very well the points determined in the GVT. Corresponding equivalent elastic displacements and torsions can be seen spanwise in Fig. 5.

With the spanwise aerodynamic properties, the strip geometry, and spanwise equivalent flexible displacements and torsions about the elastic axis, an aeroelas-

[6] The characterisation of the elastic modes in symmetric and anti-symmetric modes is merely an approximation.

Table 3 First 16 elastic modes of S15 (in order of modal frequency) determined at the GVT test campaign at the TUHH [12], in empty configuration and with fixed control surfaces, which are considered in the aeroelastic model.

#	Definition	Frequency ω_n (Hz)	Structural modal damping ξ (%)	Symmetry
1	1st bending, wings	3.29	0.55	symmetric
2	1st swing, wings and body	4.24	1.24	anti-symmetric
3	1st bending, wings	7.34	1.00	anti-symmetric
4	1st swing, wings	7.39	1.02	symmetric
5	1st torsion, body	8.07	1.75	anti-symmetric
6	1st bending, body	9.02	0.84	symmetric
7	2nd bending, wings	11.55	0.72	symmetric
8	1st swing, horizontal fin	11.72	1.34	anti-symmetric
9	1st bending, horizontal fin	13.55	0.86	anti-symmetric
10	2nd bending, wings	15.37	1.09	anti-symmetric
11	2nd bending, body	19.74	1.74	symmetric
12	2nd swing, wings and body	20.13	0.86	anti-symmetric
13	3rd bending, wings	21.02	2.06	symmetric
14	2nd swing, wings	25.32	1.98	symmetric
15	1st torsion, wings	27.87	1.26	symmetric
16	1st torsion, wings	28.99	3.01	anti-symmetric

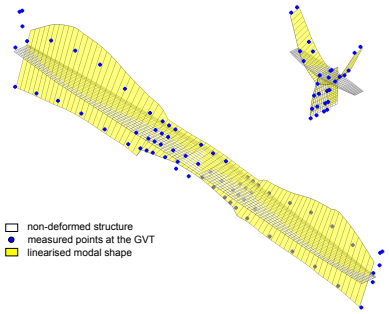

Fig. 4 Linearised modal shape of the first symmetric wing torsion and the eigenvector points from the GVT (only the modal shape's components perpendicular to the corresponding lifting surfaces are shown).

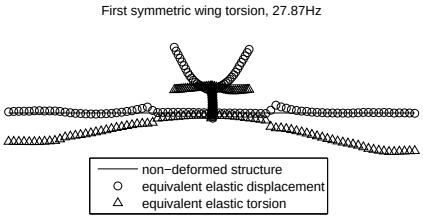

Fig. 5 Equivalent spanwise elastic displacement and torsion of the first symmetric wing torsion, used in the simulation model.

tic database can be created. The aeroelastic database enables the determination of the matrices of unsteady coefficients, given in section 2.

4 Model Validation

To validate the aeroelastic simulation program in the time domain, manoeuvres were specified to a limited portion of the aircraft flight envelope. Basically, manoeuvres adding sufficient energy into the system were chosen, while keeping the excitation amplitudes at a low level for safety reasons. Accelerometers distributed over the aircraft structure measured the structural behaviour. The results were compared to time simulation for the same (also measured) inputs and flight condition as similar as possible.

For the validation of the aeroelastic simulation model, an independent aeroelastic measurement system was integrated. The equipment consisted basically of 7 ICP (integrated circuit piezoelectric) one-dimensional accelerometers of the type 352C65 from the sensor manufacturer PCB[7], low noise cables and an acquisition system, a small portable SCADAS Recorder device from LMS[8]. The 352C65 sensor type is a miniature accelerometer with 11.2mm height and less than 10.0mm diameter, weighing only 2 grams. It measures accelerations up to $\pm$50g peak in a frequency range from 0.5 up to 10,000Hz and operates at temperatures from -54°C up to 93°C. It is ideal for applications where it is desired to add as little as possible extra weight to the test structure. The LMS SCADAS recorder is an autonomous acquisition system built on the SCADAS mobile technology [8]. The SCM05 version has up to 40 channels and a GPS antenna, and the acquired data are recorded on a compact flash card. The data can be processed later using the device in a PC front end configuration. The unity has the plant size of a laptop (345-92-300mm), weighs 6.2kg and its internal battery has 1h operation autonomy. A photo of the SCADAS Recorder is shown in Fig. 6, mounted over the co-pilot seat in S15, in a front-end configuration to program the compact flash card for the automatic recording function.

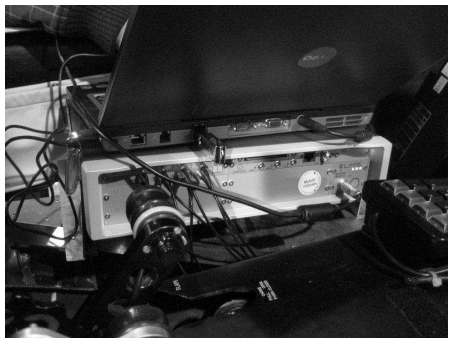

Fig. 6 SCADAS Recorder placed over the S15 co-pilot seat (here in a front-end configuration operating with a laptop to configure the compact flash card before flight)

The accelerometers were distributed in two measurement sets, namely:

[7] http://www.pcb.com/

[8] http://www.lmsintl.com/

- measurement set 1, specially for the behaviour of the wing - five sensors were placed on the left wing, organised at three different stations, including the wing tip; one sensor was mounted on the right wing tip to differentiate symmetric from anti-symmetric elastic modes; the remaining sensor, common to both measurement sets, was placed on the horizontal empennage as a link to both measurements;
- measurement set 2, specially for the behaviour of the tail - three sensors were placed on the vertical empennage, while the remaining four sensors were distributed on the horizontal empennage.

Figure 7 shows the assembly of the sensors S1 and S2 of measurement set 1, evidencing the placement details and its exact location, fixation and cable disposition, as well as the solutions to pass them through into the fuselage to the SCADAS recorder.

Fig. 7 Assembly of sensors S1 and S2 in measurement set 1 at the left wing.

(a) Sensors S1 and S2 of measurement set 1 at the left wing, laying in the connection wing-winglet. The electrical cables pass through a small duct leading to the cockpit;

(b) Sensor S1 close to the wing leading edge in detail;

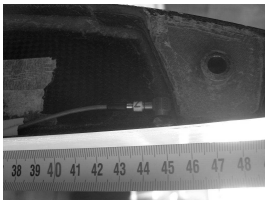

(c) Sensor S2 close to the wing trailing edge in detail.

For the excitations, the control surfaces were used. Advantage was taken of the S15's full-authority flight control system (AFCS). The desired excitation signals were programmed and their index and parameters could be selected using the reprogrammed auto-pilot control panel (AFCP), developed by TUB. As a whole, the flight test campaign used the following excitation signals:

- sinusoidal inputs of constant frequency;
- sinusoidal inputs of increasing and decreasing frequencies (sine-sweep);
- 3-2-1-1 step input.

The response at sensor S1 positioned at the left wing tip as well as the deflection at the left wing's internal flap (IL) can be seen in Fig. 8 for the sinusoidal input

using the flaps, at a constant frequency of 3.29Hz and 120km/h IAS. A very good coherence between measured and simulated acceleration at S1 in the permanent response and an almost unnoticeable phase difference can be observed.

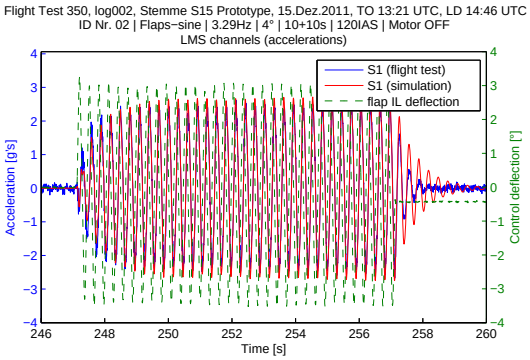

Fig. 8 S1 accelerations and flap deflection in a 3.29Hz flap sine manoeuvre at 120km/h IAS.

Overall good results were reported from the comparison of the simulated results and the flight test data. The damping factors predicted by the simulation model were lower than the damping factors determined from flight test data. Therefore it can be concluded that the model is conservative, i.e. the model is on the safe side. In general, and also considering the difficulties in calculating the damping ratios from flight test data due to signal degradation (noise for example), the values predicted by the flight simulation model can be considered satisfactory - an average of up to 80% of the measured value for modes 2 (first anti-symmetric swing, wings and fuselage) and 3 (first anti-symmetric wing bending). The amplitudes of the accelerations in the permanent excitation, regarding the flaps and ailerons, were predicted also satisfactorily, with averages under 20% error. For the rudder, important differences in amplitude appear, which die out with the flight speed, pointing out the importance of the rudder effectiveness, not considered in the model. Phase differences become important for the excitation of modes 2 and 3. The analyses of the sweep manoeuvres in the frequency domain indicated a small difference in the resonance frequencies between model and flight measurement. Small differences in frequency have a great impact on the phase.

5 Aeroservoelastic Stability Analysis

In this section, the aeroelastic model will be used to predict the influence of aircraft control on the stability of the elastic modes. Two simple examples are analysed: a yaw damper, with feedback from the yawing rate to the rudder; and a pitch damper, with feedback from the pitching rate to the elevator.

The integrated dynamic model of the flexible aircraft can be used to predict the contribution of the flexibility to the angular rates based on the position of the respective sensor. Normally the sensors that measure the angular rates are located close to the aircraft CG and at the aircraft symmetry plane, where the flexibility effects are minimal. To demonstrate the effects of the flexibility, two different hypothetical sensor locations are chosen, which are shown in Fig.9. Point P1 lies 0.67m from the aircraft symmetry plane at the right wing, and 0,60m aft from the wing leading edge. Point P2 lies at the VTP, 0.64m from the VTP leading edge, at a distance 0.16m from the fuselage.

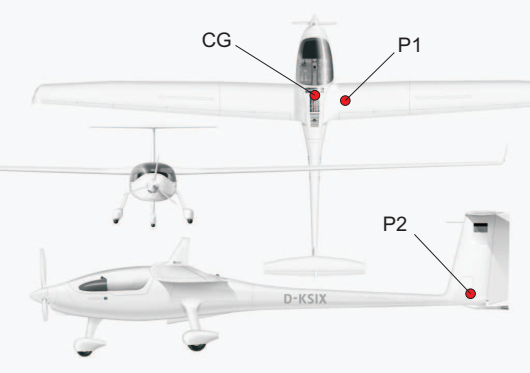

Fig. 9 Hypothetical sensor positioning to measure the aircraft angular rates.

Being $\boldsymbol{\Phi}(\mathbf{P})$ the vectorial function of the elastic displacements at a generic point $\mathbf{P}$ of the aircraft structure, the elastic contributions to the roll, pitch and yaw rates measured at this point are, respectively:

$$\begin{aligned}
\Delta p^{\text{flex}} &= \left[\frac{\partial \boldsymbol{\Phi}_z(\mathbf{P})}{\partial y} - \frac{\partial \boldsymbol{\Phi}_y(\mathbf{P})}{\partial z}\right]\dot{\boldsymbol{\eta}} \\
\Delta q^{\text{flex}} &= \left[-\frac{\partial \boldsymbol{\Phi}_z(\mathbf{P})}{\partial x} + \frac{\partial \boldsymbol{\Phi}_x(\mathbf{P})}{\partial z}\right]\dot{\boldsymbol{\eta}} \\
\Delta r^{\text{flex}} &= \left[\frac{\partial \boldsymbol{\Phi}_y(\mathbf{P})}{\partial x} - \frac{\partial \boldsymbol{\Phi}_x(\mathbf{P})}{\partial y}\right]\dot{\boldsymbol{\eta}}.
\end{aligned} \tag{9}$$

The elastic modes contribute to the angular rates at their eigen frequency. If the angular rates are fed back to the control system, there is a demand for the control system to act at the same frequencies. The result is a coupling of the control with the elastic mode, which can increase or decrease the modal damping.

For the following aeroservoelastic investigations, the aircraft was linearised at the flight condition of Tab. 4. The yaw damper is simply a feedback from the yaw rate to the rudder command, so that:

Table 4 Reference condition for aeroservoelastic investigations.

Parameter	Value	Unit
mass	1000	kg
CG position (from nose)	2.64	m
velocity (TAS)	50	m/s
altitude	1200	m
throttle	98	%
RPM	1953.5	RPM
flaps	0	°
sideslip angle	0	°
bank angle	0	°

$$\begin{aligned}\delta_{\text{rudder}} &= K_r r^{\text{sensor}} \\ &= K_r \left(r^{\text{RB}} + \Delta r^{\text{flex}} \right). \end{aligned} \tag{10}$$

Here, r^{RB} denotes the "rigid body" yaw rate, i.e. the yaw rate due to the angular motion of the aircraft without flexibility effects, while r^{sensor} is the measured yaw rate at the respective sensor, thus accounting for the flexibility effects.

Similarly, the pitch damper consists in a feedback of the pitch rate to the elevator command, so that:

$$\begin{aligned}\delta_{\text{elevator}} &= K_q q^{\text{sensor}} \\ &= K_q \left(q^{\text{RB}} + \Delta q^{\text{flex}} \right). \end{aligned} \tag{11}$$

Reaction time and filters were ignored in this demonstration. Figures 10 and 11 show the root-loci for the gain K_r varying from 0 to 1°/(°/s), for the yaw rate measurement at point P1 and P2 respectively. In the first case, the root-loci of the elastic modes remain almost unchanged as K_r increases. Point P1 lies on the wing, thus an incremental elastic yaw rate would arise from a wing swing mode. Staying close to the fuselage, rotations due to the swing mode are locally negligible. On the other side, for measurements of yaw rate at point P2, Fig. 11 shows that elastic modes 2, 8, 12 and 16 get unstable. The first anti-symmetric wing swing (mode 2) gets unstable for $K_r = 0.3°/(°/\text{s})$. This elastic mode, with a high contribution from HTP and VTP, has a great influence over Δr^{flex}. The same can also be said from modes 5 (first fuselage torsion), 8 (first swing, horizontal fin), 12 (second swing, wings and body) and 16 (first anti-symmetric wing torsion) - refer to Tab. 3 to the association of elastic mode number and mode description. In Fig. 12 the root-loci of the dutch roll mode are shown in detail, comparing both measurement points P1 and P2. No important differences are observed - for a moderately flexible aircraft, the elastic contribution to the angular rate is small compared to the body angular rate.

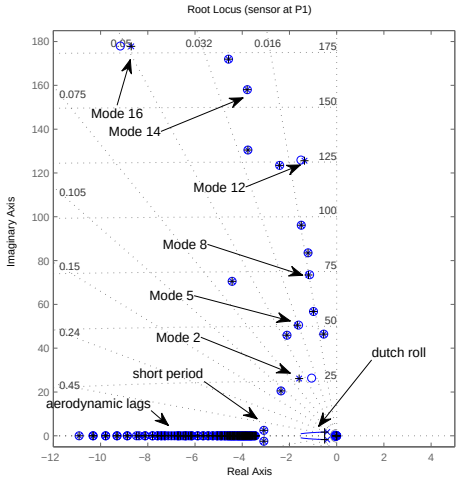

Fig. 10 Root-loci of the flexible aircraft dynamics at 50m/s with yaw damper, the gain K_r varying from 0 to 1s; the yaw rate measured from point P1. $\times$ poles; **o** zeros; $+$ $K_r = 0.1$s.

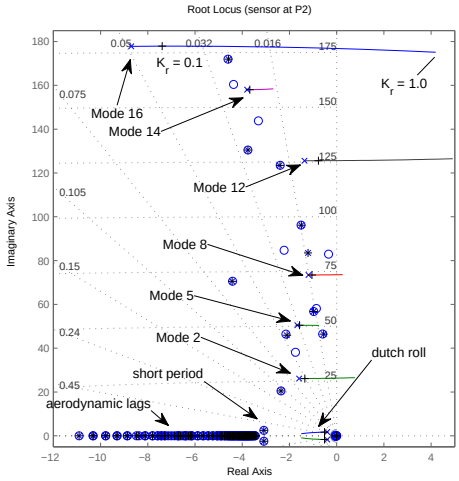

Fig. 11 Root-loci of the flexible aircraft dynamics at 50m/s with yaw damper, the gain K_r varying from 0 to 1s; the yaw rate measured from point P2. $\times$ poles; **o** zeros; $+$ $K_r = 0.1$s.

The root-loci of th e aircraft dynamics with the pitch damper are displayed in Figures 13 and 14 respectively for measurements of pitch rate at points P1 and P2. The flexibility can induce a pitch rate at point P1 by means of wing torsion or fuselage bending. At point P2, the most important effect is the fuselage bending. In Fig. 13 it can be observed that mode 6 (first symmetric fuselage bending) gets unstable (for K_q approximately 0.4°/(°/s)). Mode 14 (second symmetric wing swing) moves in the direction of the unstable region, and mode 15 (first symmetric torsion of the wings) gets more stable. Turning to Fig. 14 for point P2, mode 6 gets more stable, while mode 11 (second fuselage bending) gets unstable for K_q approximately 0.75

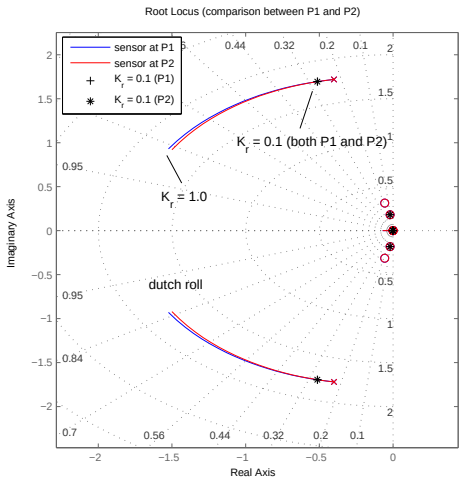

Fig. 12 Root-loci of the flexible aircraft dynamics at 50m/s with yaw damper, the gain K_r varying from 0 to 1s; comparison of low frequency root-loci for sensor positioning at P1 and P2. $\times$ poles; **o** zeros; $+$ $K_r = 0.1$s (P1); $*$ $K_r = 0.1$s (P2).

°/(°/s). The different root-loci of the elastic mode 6 are shown in Fig. 15 comparing the sensor position at P1 and P2 - observe the importance of the sensor placement. In the same figure, the root-loci of the short-period are shown, and no important differences can be observed regarding the sensor position, for the same reason discussed above for the yaw damper.

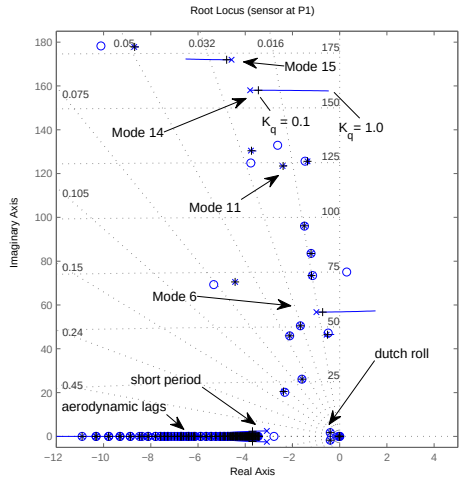

Fig. 13 Root-loci of the flexible aircraft dynamics at 50m/s with pitch damper, the gain K_q varying from 0 to 1; the pitch rate measured from point P1. $\times$ poles; **o** zeros; $+$ $K_q = 0.1$s.

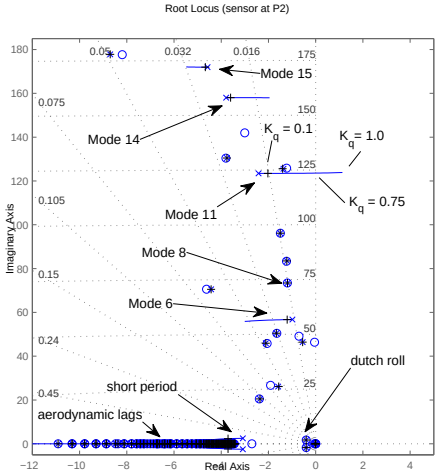

Fig. 14 Root-loci of the flexible aircraft dynamics at 50m/s with pitch damper, the gain K_q varying from 0 to 1; the pitch rate measured from point P2. $\times$ poles; **o** zeros; $+$ $K_q = 0.1$s.

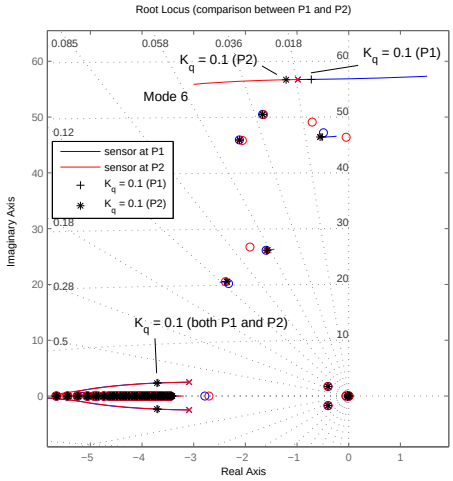

Fig. 15 Root-loci of the flexible aircraft dynamics at 50m/s with pitch damper, the gain K_q varying from 0 to 1; comparison of low frequency root-loci for sensor positioning at P1 and P2. $\times$ poles; **o** zeros; $+$ $K_q = 0.1$s (P1); $*$ $K_q = 0.1$s (P2).

6 Conclusions

This paper demonstrated the application of a methodology of modelling the dynamics of moderately flexible, high-aspect-ratio aircraft in the time domain for aeroservoelastic investigations. In the examples given in this paper, the effects of the flexibility measured by angular rate sensors were illustrated concerning the stability of the closed-loop system for an yaw and a pitch damper. It is clearly seen that feeding back a signal containing flexible contributions (at different frequencies) can

make the overall system unstable. Similarly, control could be applied to increase the damping of the elastic modes. Selecting two different sensor positions, the influence of different modes in the closed-loop system were outlined. These simple examples evidence the relevance of this methodology. Validation of this methodology with flight test results attested the fidelity of the model and therefore substantiates its applicability to this kind of problem. It is expected that this methodology will be used to assist the control law design for the class of aircraft discussed here.

7 Acknowledgements

This work was developed at the Technical University of Berlin (TUB) with assistance of STEMME AG and the Technical University of Hamburg-Harburg (TUHH), with a scholarship from the German Academic Exchange Service (DAAD). The author is very thankful to these organisations for the support, as well as to Prof. Dr.-Ing. Robert Luckner (TUB) for his technical supervision.

References

1. Wagner H (1925) Über die Entstehung des dynamischen Auftriebes von Tragflügeln. Zeitschrift für angewandte Mathematik und Mechanik, doi: 10.1002/zamm.19250050103
2. Milne RD (1964) Dynamics of the Deformable Aeroplane. Her Majesty's Stationary Office, url: http://aerade.cranfield.ac.uk/ara/arc/rm/3345.pdf
3. Waszak MR, Schmidt DK (1988) Flight Dynamics of Aeroelastic Vehicles. Journal of Aircraft, doi: 10.2514/3.45623
4. Noll TE, Eastep FE (1995) Active Flexible Wing Program (Editorial). Journal of Aircraft, doi: 10.2514/3.56918
5. Pery III B, Cole SR, Miller GD (1995) Summary of an Active Flexible Wing Program. Journal of Aircraft, doi: 10.2514/3.46677
6. Bisplinghoff RL, Ashley H, Halfman RL (1996) Aeroelasticity. Dover Publ., Mineola, NY, USA, ISBN: 0-486-69189-6
7. Fielding C, Luckner R (2000) Industrial Considerations for Flight Control, doi: 10.2514/5.9781600866555.0001.0055
8. LMS (2007) LMS SCADAS Mobile: User and Installation Manual. LMS International, url: http://www.lmsintl.com/
9. Krüger W (2008) Neue Bauweisen, neue Konfigurationen, neue Fragen: Herausforderungen für die Aeroelastische Simulation. Kolloquium zum Abschied von Prof. Hönlinger, url: http://elib.dlr.de/56117/
10. Looye GHN (2008) An Integrated Approach to Aircraft Modelling and Flight Control Law Design. PhD. Dissertation, Technische Universiteit Delft, ISBN: 978-90-5335-148-2
11. Silvestre FJ (2008) Dynamics and Control of a Flexible Aircraft. Proceedings of the AIAA Atmospheric Flight Mechanics Conference and Exhibit, Honolulu, Hawaii, USA
12. Weltin U (2008) Flattersicherheit S6T. Internal Report (not published), Technische Universität Hamburg-Harburg (reserved)
13. Danowsky BP, Thompson PM, Farhat C, Lieu T, Harris C, Lechniak J (2010) Incorporation of Feedback Control into a High-Fidelity Aeroservoelastic Fighter Aircraft Model, doi: 10.2514/1.47119

14. Rudenko A (2010) Experimentelle Bestimmung der Massenträgheitsmomente eines Kleinflugzeuges mit Hilfe eines Pendelversuches unter Anwendung numerischer Methoden der Systemidentifikation. Abschlussarbeit an der Technischen Universität Berlin
15. Meyer-Brügel W, Luckner R (2011) Flight Mechanical Simulation Models for Design and Test of Automatic Flight Control Functions. Proceedings of the CEAS EURO GNC 2011 Conference, München, Germany
16. Silvestre FJ (2012) Methodology for Modelling the Dynamics of Moderately Flexible, High-Aspect-Ratio Aircraft in the Time Domain for Aeroservoelastic Investigations. Doctoral Thesis at TU Berlin, Berlin, Germany
17. Dalldorff L, Luckner R, Reickel R (2013) A Full-Authority Automatic Flight Control System for the Civil Airborne Utility Aircraft S15 - LAPAZ. 2nd Euro GNC 2013, Delft, The Netherlands